*Jordan Journal of Civil Engineering*, Volume **20**, No. **2**, **2026**
**DOI:** https://doi.org/10.14525/JJCE.v20i2.08

**Jordan Journal of Civil Engineering**

**Journal homepage:** https://jjce.just.edu.jo

# Numerical Simulation of Concrete Damage Evolution in Concrete Slabs under Axial Loading of Batter Piles

***Honghui Mao*** [1)], ***Kaichen Zhu*** [2)*], ***Lei hu*** [1)], ***Shiyong Shi*** [1)], ***Qianhao Wang*** [3)], ***Junneng Ye*** [4)]

[1)] *Ningbo Ningda Foundation Treatment Technology Co., Ltd., Ningbo 315211, China.*
[2)] *Ningbo Tech University, Ningbo 315100, China. *Corresponding Author. E-Mail: 1123893328@qq.com*
[3)] *Zhejiang Hongchen Construction Co., Ltd., Ningbo 315032, China.*
[4)] *Ningbo Rail Transit Group Co., Ltd. Ningbo 31501, China.*

ARTICLE INFO

*Article History:*
Received: 22/1/2025
Accepted: 3/11/2025

ABSTRACT

This paper investigates concrete slab cracking induced by embedded composite batter piles within structural slabs. Utilizing finite-element analysis and concrete plastic damage theory, a computational model of the concrete slab-pile interaction was developed. The results showed that the tensile damage of the concrete slab concrete exhibits a spatial distribution characteristic, with early and high damage near the top and bottom surfaces and lower damage in the middle. Vertical cross-sections reveal damage concentration on the pile hole sidewalls adjacent to the top surface. Plan views demonstrate that damage initiates first at the slab top surface adjacent to the pile hole perimeter. Subsequent load increases intensify damage along the hole walls, ultimately leading to brittle cracking. Severe damage in the form of an arc occurs on the bottom surface of the slab on both sides of the hole. Although the waterproof steel plate effectively inhibits vertical tensile damage progression along the hole walls, it does not prevent damage development on the top and bottom surfaces of the slab. These findings hold a significant value for engineering practice.

***Keywords:*** Concrete slab, Stress concentration, Concrete plastic damage, Finite-element method.

## INTRODUCTION

In recent years, the increasing development of underground projects and high-rise buildings has increased focus on the design and implementation of deep foundation pit enclosure structures. Conventional internal support systems are often constrained by limited spatial capacity, prolonged construction timelines, significant environmental impacts, and poor cost-effectiveness. While double-row pile supports are widely adopted, their economic efficiency and deformation control capabilities remain limited, particularly in deep foundation pits within soft soil areas. Although anchor rod systems offer lower costs, their usage is restricted to certain regions due to potential adverse environmental impacts. Consequently, the self-stabilizing batter pile enclosure system has gained wide popularity in the Yangtze River Delta region, owing to its efficient construction process and favorable economic benefits; a simplified schematic diagram is shown in Figure 1(a) (Zheng et al., 2019; Shi et al., 2023; Xu, 2024).

To meet strict deformation control requirements in foundation pit support, initial designs select high-bearing-capacity batter piles for effective lateral displacement restraint. After the foundation slab/wall is

poured, these piles are truncated: the section above the slab is removed while the embedded portion retains its supporting function. This truncation transfers the pile's axial load to the slab-pile interface, inducing stress re-distribution. Subsequent superstructure loading intensifies stress interactions at slab openings, resulting in complex tensile-shear stress fields. Given concrete's low tensile strength, such stress concentrations make the opening periphery vulnerable to tensile damage and crack propagation, with potential structural integrity compromise. In a Ningbo foundation pit project using composite batter piles, cracking occurred in the mat foundation concrete adjacent to truncated pile walls after removal (Fig. 1(b)).

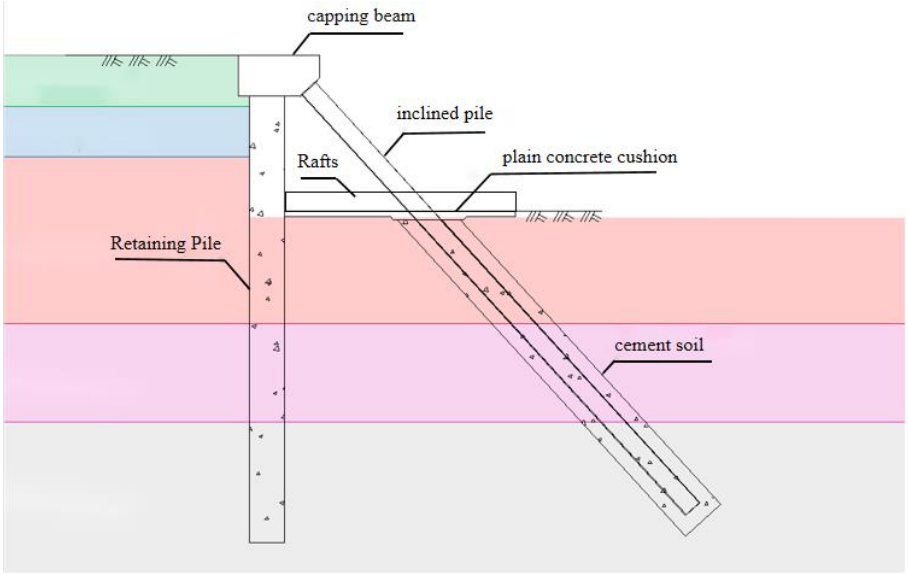


(a) Section of SCDM piles in the pit

(b) Cracked concrete slab at construction sit

**Figure 1.** Section of SCDM piles in the pit and cracked concrete

Understanding internationally the punching shear failure mode in slab-column connections continues to advance. Early seminal research (Moe, 1961; Kinnunen & Nylander, 1960) attributed the failure to critical shear failure, characterized by inclined cracks propagating from the mid-region of the slab towards the compression/tension zones, ultimately forming a punching cone. Recent advances in testing technology have revealed additional failure morphologies: Wu et al. (2022), utilizing industrial endoscopes, observed splitting failure within the decompressed concrete zone, manifested by a sudden drop in radial strain in the compression zone concrete, accompanied by horizontal tearing cracks. Classen et al. (2023) further elucidated the mechanism of coexistence between splitting failure and critical shear failure.

Current design codes ACI318 and MC2013 existing research on punching shear failure primarily address vertical slab-column connections. In practical engineering applications, however, steel pipe composite piles frequently connect to slabs at an inclination. Furthermore, significant structural configuration

differences exist between concrete-encased steel pipe joints with integrated waterproof steel plates and monolithic cast-in-place slab-column connections. Given the increasing adoption of this technique in soft soil regions, scientifically evaluating batter pile-induced punching shear damage is critical for optimizing construction methods and ensuring structural safety.

This paper established a finite-element model of steel pipe composite piles precast at defined inclination angles within concrete slabs, utilizing the Concrete Damage Plasticity (CDP) constitutive model. The model was employed to investigate the evolution of concrete damage and interfacial failure modes at the pile-slab interface under monotonic axial loading. Through comparative modeling, the mitigating effect of weld-attached impermeable steel plates on the steel pipes against concrete damage progression was quantified. The findings offer viable design optimization strategies for this category of engineering structures.

**Concrete Plastic Damage Model**

The Concrete Damage Plasticity model was proposed by Lubliner et al. (1988) and improved by Lee and Fenves. (1998). Three main constitutive models for concrete materials in finite-element analysis applications are: (1) the brittle cracking model; (2) the smeared cracking model; (3) the damaged plasticity model. Among these, the concrete damaged plasticity model is the most commonly used. In terms of research on concrete plastic damage models, Nie and Wang (2013) studied and compared the smeared cracking model and plastic damage model in ABAQUS. The results showed that the ABAQUS concrete plastic damage model can better reflect concrete cracking. This model has been widely adopted by researchers in civil engineering (Hu et al., 2021; Li & Zhao., 2023; Wang et al., 2025; Hemzah, S.A. et al., 2019).

**Stress-Strain Relationship in the Concrete Plastic Damage Model**

As shown in Figure 2(a), under uniaxial tension, the concrete is in the linear elastic stage before reaching $\sigma_{t0}$. After that, the concrete enters the softening stage and its stiffness decreases. $\tilde{\varepsilon}_t^{ck}$ is the cracking strain, $\varepsilon_{0t}^{el}$ is the elastic strain under the initial stiffness, $\tilde{\varepsilon}_t^{pl}$ is the tensile equivalent plastic strain, and $d_t$ is the tensile damage factor. The relationship between stress, strain and cracking strain can be described by Equations from (1) to (3):

$$\tilde{\varepsilon}_t^{ck} = \varepsilon - \varepsilon_{0t}^{el} \tag{1}$$

$$\varepsilon_{0t}^{el} = \frac{\sigma_t}{E_0} \tag{2}$$

$$\tilde{\varepsilon}_t^{pl} = \tilde{\varepsilon}_t^{ck} - \frac{d_t}{1-d_t}\frac{\sigma_t}{E_0} \tag{3}$$

As shown in Figure 2(b), under uniaxial compression, the material is in the linear elastic response stage before reaching $\sigma_{c0}$. As the stress increases, it enters the $\sigma_{c0}$ to $\sigma_{cu}$ region, and the concrete exhibits hardening characteristics. Subsequently, the material gradually transitions to the softening stage. In this figure, the symbol $\tilde{\varepsilon}_c^{in}$ represents the inelastic strain component, $\varepsilon_{0c}^{el}$ represents the elastic strain calculated based on the initial stiffness, $\tilde{\varepsilon}_c^{pl}$ is marked as the equivalent plastic strain in compression, and $d_c$ represents the compression damage factor. The intrinsic relationship between stress, strain and inelastic strain can be expressed by Equations from (4) to (6).

$$\tilde{\varepsilon}_c^{in} = \varepsilon - \varepsilon_{0c}^{el} \tag{4}$$

$$\varepsilon_{0c}^{el} = \frac{\sigma_c}{E_0} \tag{5}$$

$$\tilde{\varepsilon}_c^{pl} = \tilde{\varepsilon}_c^{in} - \frac{d_c}{1-d_c}\frac{\sigma_c}{E_0} \tag{6}$$

**Constitutive Relationship of Concrete for Concrete Slabs**

The concrete constitutive relationship refers to the stress-strain curve equation given in GB 50010-2010 'Code for Design of Concrete Structures'. The concrete uniaxial compression stress-strain curve is determined according to Equations from (7) to (11), where $d_c'$ is the concrete uniaxial compression damage evolution parameter, the uniaxial compressive strength $f_{c,r}$ corresponds to the peak compressive strain of the concrete $\varepsilon_{c,r} = \left(700 + 172\sqrt{f_c}\right) \times 10^{-6}$, and the parameter value $\alpha_c = 0.157 f_c^{0.785} - 0.905$ defines the descending section of the concrete uniaxial compression stress-strain curve.

$$\sigma = (1 - d_c')\mathrm{E_c}\varepsilon \tag{7}$$

$$d_c' = \begin{cases} 1 - \dfrac{\rho_c n}{n - 1 + x^n} & x \leqslant 1 \\ 1 - \dfrac{\rho_c}{\alpha_c (x-1)^2 + x} & x > 1 \end{cases} \tag{8}$$

$$\rho_c = \frac{f_{c,r}}{E_c \varepsilon_{c,r}} \tag{9}$$

$$n = \frac{E_c \varepsilon_{c,r}}{E_c \varepsilon_{c,r} - f_{c,r}} \tag{10}$$

$$x = \frac{\varepsilon}{\varepsilon_{c,r}} \tag{11}$$

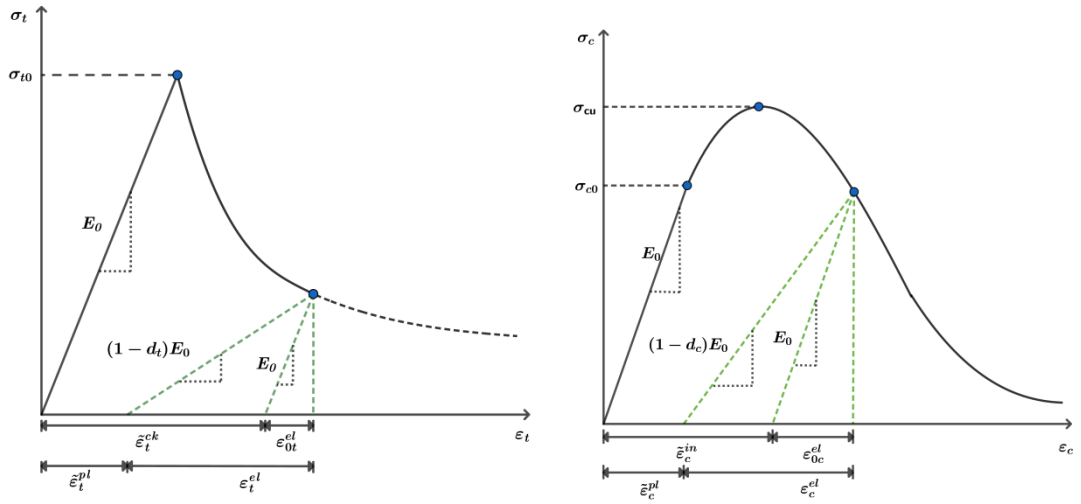


(a) uniaxial tension (b) uniaxial compression

**Figure 2.** Concrete uniaxial tension/compression stress-strain curve

The concrete uniaxial tension stress-strain curve is determined according to Equations from (12)-(15).$d_t'$ is the concrete uniaxial tension damage evolution parameter, where the uniaxial tensile strength $f_{c,r}$ corresponds to the peak tensile strain $\varepsilon_{t,r} = f_{t,r}^{0.54} \times 65 \times 10^{-6}$ of the concrete, and the parameter value $\alpha_t = 0.312 f_{t,r}^2$ of the descending section of the concrete uniaxial tension stress-strain curve.

$$\sigma = (1 - d_t') E_c \varepsilon \tag{12}$$

$$d_t' = \begin{cases} 1 - \rho_t [1.2 - 0.2x^5] & x \leqslant 1 \\ 1 - \dfrac{\rho_t}{\alpha_t (x-1)^{1.7} + x} & x > 1 \end{cases} \tag{13}$$

$$x = \frac{\varepsilon}{\varepsilon_{t,r}} \tag{14}$$

$$\rho_t = \frac{f_{t,r}}{E_c \varepsilon_{t,r}} \tag{15}$$

Damage evolution parameters specified in current standards cannot be directly implemented in finite-element software. Sidoroff (1980) postulated the principle of energy equivalence, which asserts that damaged and undamaged materials exhibit identical elastic strain energy density under equivalent stress states. This study computes the damage factor using the following expression:

$$d = 1 - \sqrt{\frac{\sigma}{E_0 \varepsilon}} \tag{16}$$

Damage parameters for ABAQUS simulations can be determined through Eq. (16) in conjunction with the concrete constitutive model. The CDP model needs to specify the dilation angle ψ, eccentricity e, ratio of the biaxial to uniaxial compressive yield stress $f_{b0}/f_{c0}$, the ratio K of the constant stress between the tensile meridian and the compressive meridian and the viscosity parameter μ. The larger this parameter is, the easier the calculation will converge; the smaller it is, the higher the calculation accuracy. The plastic parameters for this numerical calculation are taken from Table 1.

**Table 1. CDP model plasticity parameters**

| Ψ | e | $f_{b0}/f_{c0}$ | K | μ |
|---|---|---|---|---|
| 30° | 0.1 | 1.16 | 0.6667 | 0.0005 |

**Finite-element Model for Plate-Pile Structures**

Figure 3(a) shows the assembled model. For the batter pile component, both the cement soil infill inside the steel pipe and the outer core cement soil are modelled using an elastic constitutive model to describe their mechanical behaviors, and the material properties of the two cement soils are set to be consistent. The specific specifications of the steel pipe are: diameter 325 mm, thickness 10 mm, total length 25 m. A waterproof steel plate (600mm × 600 mm × 4 mm) is welded to the mid-height of the steel pipe at the interface with the concrete. The diameter of the reinforcement is set to 22 mm, and it is arranged in a double-layer bidirectional manner, with a spacing of 150 mm between layers and rows. The steel pipes (including welded plates), reinforcement, and waterproof steel plates are all made of steel with a yield strength of 400 MPa, and the mechanical behaviors of these steels is described using a bilinear constitutive model. Table 2 lists the detailed material property parameters.

**Table 2. Material property parameters**

| Material | Density ($kg/m^3$) | Young's modulus (GPa) | Poisson's ratio |
|---|---|---|---|
| Concrete | 2500 | 30 | 0.2 |
| Steel | 7800 | 200 | 0.3 |
| Cement soil | 2000 | 0.2 | 0.3 |
| Waterproof steel plate | 7800 | 200 | 0.3 |

Figure 3(b) shows the finite-element mesh of the main analysis area. Balancing computational accuracy and cost, the model was meshed uniformly along its thickness direction, with the element size controlled at 50 mm, while the element size in the plane of the plate was in the range of 50 mm to 180 mm. Reinforcement was modeled using T3D2 truss elements, capable of resisting tension or compression. Their cross-sectional area was defined in the property settings. The steel pipes and waterproof steel plate were modelled using S4R four-node elements, and the shell thickness was specified in the cross-section definition section of the property settings. As for the concrete and cement-soil components, they were all meshed using C3D8R eight-node elements.

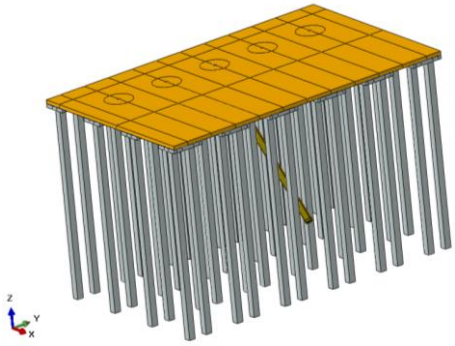

(a) Overall model diagram

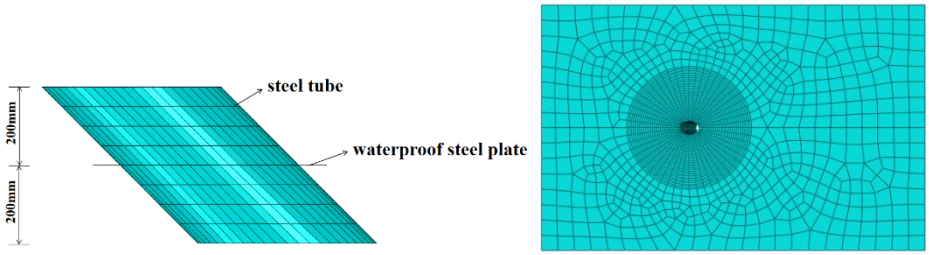


(b) Finite-element mesh element diagram of the main analysis area

**Figure 3.** Finite-element mode

Constraints were applied to the perimeter of the concrete slab to restrict horizontal displacement at the boundaries. Assuming perfect bond between the reinforcement, waterproof steel plate, and concrete, the 'embedded' constraint method was used to embed the reinforcement and waterproof steel plate within the concrete solid. 'Tie' constraints were applied at the interfaces between the raft and the bearing platform, the contact interface between the raft hole and the steel pipe, and the contact interface between the steel pipe and the cement soil. This ensured that these interfaces remained connected without separation during the simulation. To investigate the cracking failure mode of concrete slabs under pile-slab interaction, the distributed soil resistance was simplified to a concentrated axial load of 1440 kN applied at the pile tip. This load magnitude corresponds to the design axial force from the superstructure. This setup primarily simulates the scenario where, under ideal axial loading conditions, the load is transferred to the concrete slab after the inclined pile is severed.

## RESULTS AND DISCUSSION

### Analysis of Tensile Damage in the Vertical Direction of the Concrete Slab

Figure 4(a) and Table 1 show the damage evolution across concrete slab layers from 1 to 8 under loading, revealing variations between layers and propagation patterns. During initial loading, all layers remained in the linear elastic stage. Tensile damage increased nearly linearly with stress at low magnitude. As loading increased, localized regions within each layer sequentially attained the tensile strength (Table 1), signifying a transition to damage development initiated by stress concentrations at the pile-slab interface. This is evidenced by the stress visualization in Figure 4(b). Damage propagated top-down from the surface layer inward. This behavior resembles that of typical slab-column joints, where cracks initiate at the interface and propagate into the slab (SANTA RITA SIMÕES, J.T.R.B., 2018). Data in Table 3 indicates that both damage initiation and the attainment of critical damage (dt=0.9) first occurred in Layer 1, followed sequentially by Layers from 2 to 4. The physical mechanism involves stress concentrations at the pile-slab interface triggering micro-cracking in Layer-1 concrete, with resultant stress redistribution transferring loads to deeper layers. Although damage initiation was detected in intermediate Layers 5 and 6, these layers did not reach dt=0.9 within the applied load range (Fig. 4(c)), further evidencing the progressive failure mode from the surface inward. Damage in Layers 7 and 8 will be discussed in the planar damage analysis.

**Table 3. Critical load (kN) for concrete damage growth**

| layer | Non-linear damage development | $d_t = 0.9$ |
|---|---|---|
| 1 | 480 | 880 |
| 2 | 520 | 960 |
| 3 | 580 | 1000 |
| 4 | 680 | 1250 |
| 5 | 750 | - |
| 6 | 880 | - |
| 7 | 790 | - |
| 8 | 720 | 1250 |

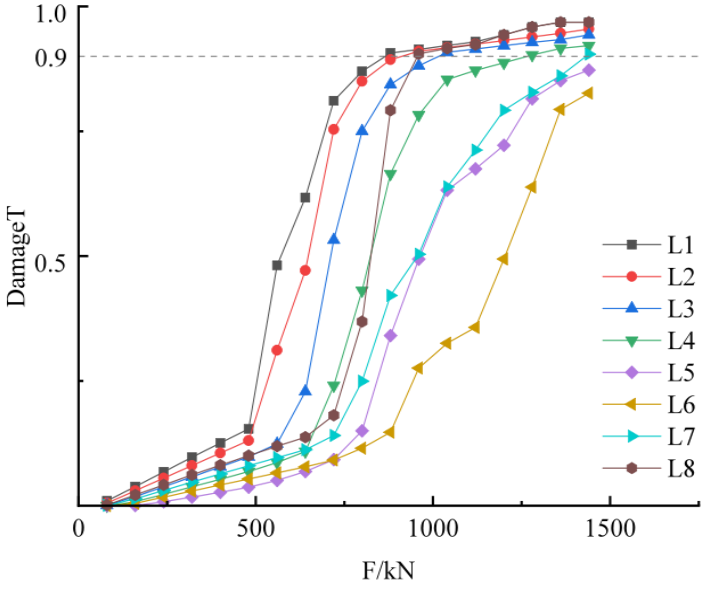


(a) Load-tensile damage diagram for each layer of the concrete slab

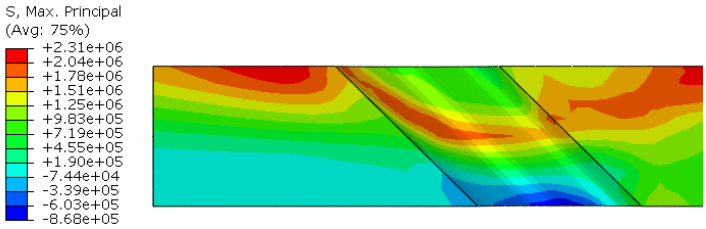


(b) Stress contour map at 880-kN load

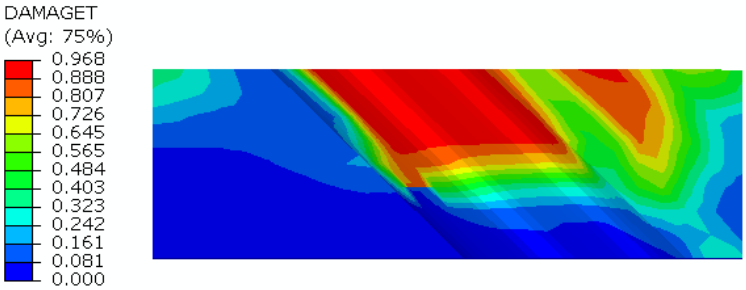


(c)Tensile damage distribution in the vertical section of a concrete slab at 1440-kN load

**Figure 4.** Tensile damage in the vertical direction of the concrete slab with waterproof steel plate

**Plane Tensile Damage Analysis of the Concrete Slab**

Analysis of vertical damage in concrete slabs indicates that the top and bottom regions experience earlier damage initiation and exhibit higher final tensile damage values. This section examines damage development and the distribution of severely damaged areas in the slab's top and bottom regions under specific loads, based on the contour plot in Figure 5.

Damage distribution at the slab top under loads of 880 kN and 1440 kN (Figure 5(a)) shows that tensile damage initiates near the pile hole wall and propagates radially outward from the pile hole center. At 1440 kN, damage progression continues circumferentially along the pile hole curvature, and a radial damage zone develops. This distribution pattern closely corresponds to the actual concrete slab cracking pattern (Fig. 1(b)), validating the model's accuracy.

Figure 5(b) illustrates damage distribution at the slab bottom under identical loading conditions. In contrast to the top surface, damage is concentrated around the pile. At 880 kN, an annular damage zone develops adjacent to the pile hole periphery. Under 1440 kN loading, tensile damage extends symmetrically through arcuate zones flanking the pile hole (Fig. 6). The slab in this

region is constrained by the piles, causing upward bulging, which induces stress concentration and exacerbates damage.

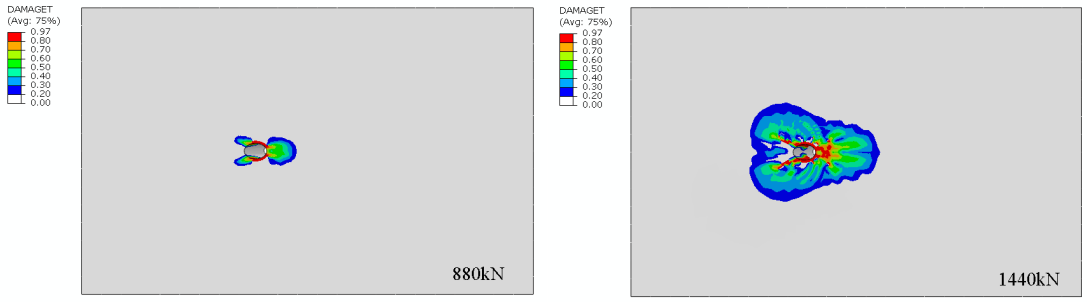


(a) Top of the concrete slab

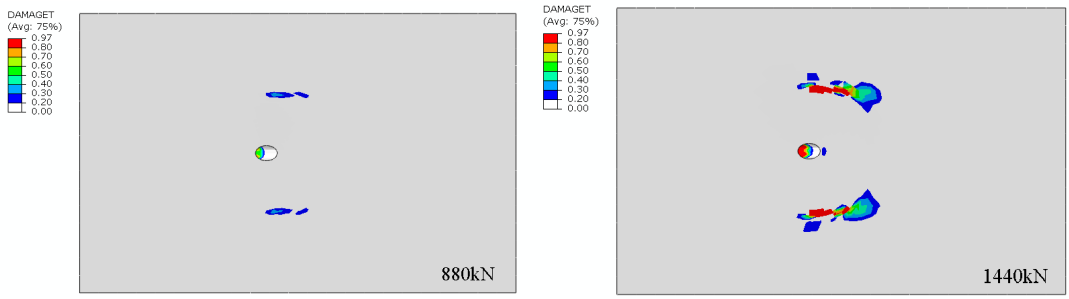


(b) Bottom of the concrete slab

**Figure 5.** Tensile damage contour maps at loads of 880 kN and 1440 kN

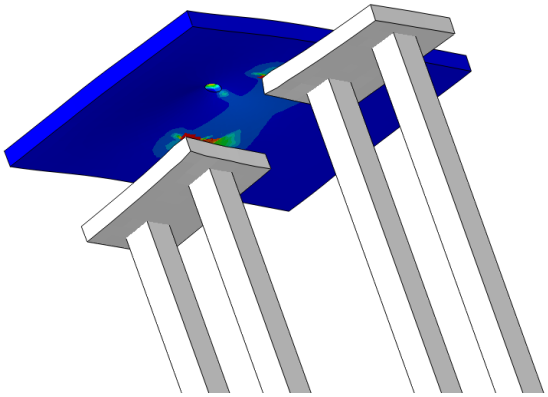

**Figure 6.** Distribution of tensile damage at the bottom of the concrete slab

**Analysis of the Influence of the Waterproof Steel Plate**

A comparative analysis was performed between two models: one incorporating the waterproof steel plate and one without. Figure 7(a) shows the maximum tensile damage in each concrete layer for the model without the waterproof steel plate. Except for Layers 4 and 5, the damage progression in other layers followed a trend similar to the model with the waterproof steel plate. However, Layers 4 and 5 in the model without the plate exhibited a higher rate of tensile damage growth and greater peak damage values (Fig. 8(a)). Figure 7(b) shows the distribution of severe tensile damage along the axial profile of the pile hole without a waterproof steel plate. Damage is concentrated in layers from 1 to 4 along the pile hole wall. In contrast, tensile damage in the layer-4 sidewall of the model with the waterproof steel plate (Fig. 4(c)) is significantly less severe. As shown in Figure 8(b), the pile load-displacement curves for both simulations are compared. Prior to reaching 880 kN, the displacement response to the applied load was linear elastic, and the curves for both models were nearly identical. However, at 1440 kN, the pile displacement reached 1.52 mm in the model without the waterproof steel plate, compared to 1.43 mm in the model incorporating the plate.

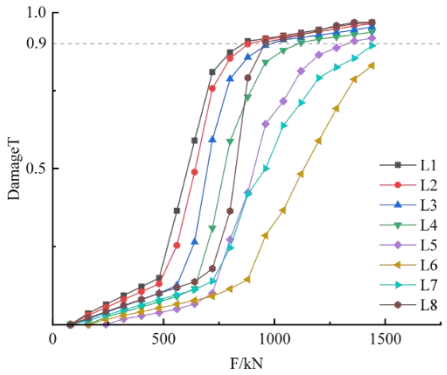


(a) Distribution of tensile damage at the bottom of the concrete slab

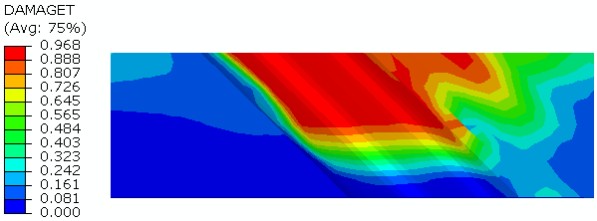


(b) Tensile damage distribution in the vertical section of a concrete slab at 1440 kN

**Figure 7.** Tensile damage in the vertical direction of the concrete slab without waterproof steel plate

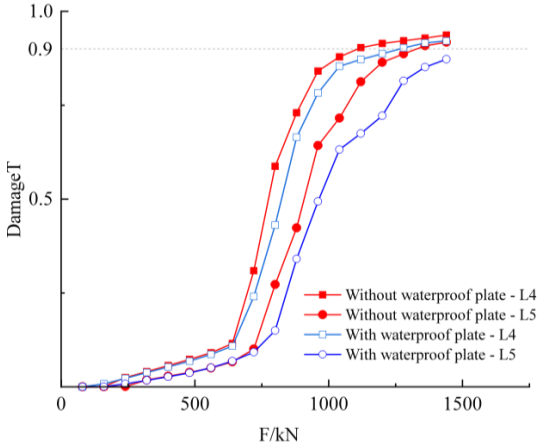


(a) Comparison of tensile damage of concrete in the fourth and fifth layers

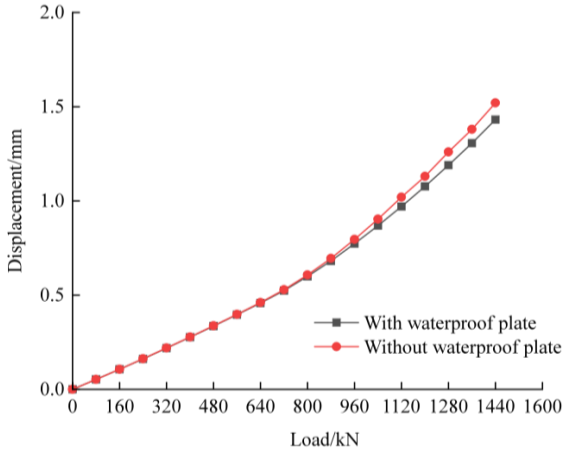


(b) Load-displacement comparison of piles

**Figure 8.** Comparison of results under two operating conditions

The steel plate, welded to the pipe and abutting the concrete, establishes an auxiliary radial load transfer

path. This mechanism partially transfers the axial pile load laterally to the surrounding concrete, consequently reducing both the interface shear stress and the radial tensile stress transmitted deeper along the interface. Consequently, this mechanism slows damage progression, reducing both the magnitude and spatial extent of damage in the intermediate layers. The resultant reduction in concrete damage also contributes to decreased displacement response.

## CONCLUSIONS

This paper developed a plastic damage model to characterize concrete slab-steel pipe pile interactions using finite-element analysis integrated with concrete plastic damage theory. The main conclusions are:

(1) Tensile damage initiates at the pile hole sidewalls, with Layer 1 starting at 480 kN and failing at 880 kN, and propagates radially outward and inward from the top surface. This failure mode corresponds well with field-observed cracking.

(2) As the load increases, the maximum tensile damage in each concrete layer evolves in three stages: initial near-linear growth, followed by rapid acceleration, culminating in a deceleration of the damage growth rate as the damage value approaches 0.9.

(3) Tensile damage develops inward from the top surface. Under 1440 kN loading, damage was predominantly distributed within the upper half (Layers 1-4) of the slab thickness. To enhance punching shear resistance, engineering practice may consider placing an additional reinforcement in the upper portion.

(4) The waterproof steel plate alters the stress transfer path. It reduced tensile damage in Layer 4 by 42% and decreased pile head displacement by 5.9%, demonstrating its effectiveness in mitigating damage in the mid-height region of the pile hole wall.

(5) The CDP model was calibrated based on static test parameters. Future research should investigate the influence of concrete strain-rate effects. The ideal axial force fails to reflect the complex stresses actually experienced by the pile body, and the “tie” connection between the steel pipe and concrete amplifies stress concentration. A more refined model is required for further investigation.

## REFERENCES


ACI 318 Committee. (2019). *Building code requirements for structural concrete (ACI 318-19) and commentary (ACI 318R-19).* American Concrete Institute, Farmington Hills, MI, USA.

Classen, M., & Kalus, M. (2023). Punching shear response theory (PSRT): A two-degree-of-freedom kinematic theory for modeling the entire punching shear vs. deformation response of RC slabs and footings. *Engineering Structures*, 116197.

Fib. (2013). *Fib model code for concrete structures 2013.* International Federation for Structural Concrete, Lausanne, Switzerland.

Hemzah, S.A., Al-Obaidi, S., & Salim, T. (2019). Punching shear model for normal and high-strength concrete slabs reinforced with CFRP or steel bars. *Jordan Journal of Civil Engineering, 13*(2), 250-268.

Hu, L.M., Liu, Z.P., Zeng, Y., & Huan, H. (2021). Stress and damage analysis of wind turbine foundation reinforcement based on ABAQUS. *Water Resources and Hydropower Engineering*, *52*(5), 223-233.

Kinnunen, S., & Nylander, H. (1960). *Punching of concrete slabs without shear reinforcement* (PhD Thesis). Royal Institute of Technology, Stockholm, Sweden.

Lee, J., & Fenves, G.L. (1998). Plastic-damage model for cyclic loading of concrete structures. *Journal of Engineering Mechanics, 124*(8), 892-900.

Li, S., & Zhao, Z.Z. (2023). Numerical simulation of seismic behavior of earthquake-damaged RC columns strengthened with FRP. *Engineering Mechanics, 40*(10), 89-98.

Lubliner, J., Oliver, J., Oller, S., & Oñate, E. (1989). A plastic-damage model for concrete. *International Journal of Solids and Structures, 25*(3), 299-326.

Ministry of Housing and Urban-Rural Development. (2015). *GB 50010-2010: Code for design of concrete structures.* China Architecture & Building Press.

Moe, J. (1961). *Shearing strength of reinforced concrete slabs and footings under concentrated loads* (PhD Thesis). Portland Cement Association, Illinois, USA.

Nie, J.G., & Wang, Y.H. (2013). Comparison study of constitutive model of concrete in ABAQUS for static analysis of structures. *Engineering Mechanics, 30*(4), 59-67.

Santa Rita Simões, J.T.R.B. (2018). *The mechanics of*

*punching in reinforced concrete slabs and footings without shear reinforcement* (PhD Thesis). École Polytechnique Fédérale de Lausanne.

Shi, S.Y., Wang, Q.H., Tao, Z., & Hua, J.Y. (2023). Construction of synchronous concentric preloaded composite batter support pile. *Building Construction*, *45*(5), 856-857.

Sidoroff, I. (1980). A theory of damage mechanics for viscoelastic materials. *International Journal of Solids and Structures*, *16*(5), 409-426.

Wang, X.C., Sun, X.J., & Li, G.C. (2025). Study on mechanical behavior of deep-buried concrete cut-off wall in dam foundation based on plastic damage model. *Water Resources and Power*, *1*, 122-126.

Wu, Y.F., Chen, H., Peng, F. et al. (2022). Experimental investigation on punching shear mechanism of concrete interior slab-column connections without shear reinforcement. *Journal of Structural Engineering*, *148*(2), 04021250.

Xu, F. (2024). Application of self-stabilizing grouting steel pipe front support technique in deep and large excavations. *Geotechnical Investigation & Surveying*, *52*(11), 32-38.

Zhen, X.Y., & Zhang, Z. (2019). Analysis of application of the advanced grouting steel pipe diagonal brace. *Construction Quality*, *37*(1), 69-72.